AGU ADVANCING EARTH AND SPACE SCIENCES

Geophysical Research Letters®

RESEARCH LETTER
10.1029/2023GL104824

Estimating Fire Radiative Power Using Weather Radar Products for Wildfires

P. E. Saide[1,2], M. Krishna[1,3], X. Ye[1,4], L. H. Thapa[1], F. Turney[1], C. Howes[1], and C. C. Schmidt[5]

[1]Department of Atmospheric and Oceanic Sciences, University of California, Los Angeles, Los Angeles, CA, USA, [2]Institute of the Environment and Sustainability, University of California, Los Angeles, Los Angeles, CA, USA, [3]Department of Earth Sciences, Dartmouth College, Hanover, NH, USA, [4]Institute of Urban Environment, Chinese Academy of Sciences, Xiamen, China, [5]Space and Science Engineering Center, Cooperative Institute for Meteorological Satellites Studies, University of Wisconsin-Madison, Madison, WI, USA

Abstract Satellite-based Fire radiative power (FRP) retrievals are used to track wildfire activity but are sometimes not possible or have large uncertainties. Here, we show that weather radar products including composite and base reflectivity and equivalent rainfall integrated in the vicinity of the fires show strong correlation with hourly FRP for multiple fires during 2019–2020. Correlation decreases when radar beams are blocked by topography and when there is significant ground clutter (GC) and anomalous propagation (AP). GC/AP can be effectively removed using a machine learning classifier trained with radar retrieved correlation coefficient, velocity, and spectrum width. We find a power-law best describes the relationship between radar products and FRP for multiple fires combined (0.67–0.76 R^2). Radar-based FRP estimates can be used to fill gaps in satellite FRP created by cloud cover and show great potential to overcome satellite FRP biases occurring during extreme fire events.

Plain Language Summary The radiant energy emitted by wildfires (FRP) is an important variable that controls many aspects of the smoke plume including the amount of emission released into the atmosphere and how high it travels. Biomass burning debris, which are large particles generated by combustion, can be suspended in the atmosphere along with smoke. Weather radars can detect and retrieve information from these large particles, which can be used for a variety of applications. In this work, we show that retrievals from weather radars can be used to estimate FRP with reasonable results. Echoes associated with ground artifacts affect these results but can be effectively screened using machine learning algorithms trained on manually selected data of representative plume and non-plume cases. Satellite FRP can often be missing or underpredicted especially for extreme fire events, and thus this technique offers an alternative way to provide a more accurate depiction of fire evolution that can be used to predict smoke impacts.

Key Points:

- Weather radar products integrated in the vicinity of fires can be used to estimate Fire radiative power (FRP) through a power-law relationship
- The relationships between FRP and radar products are skillful only after removing artifacts using a machine learning classifier
- Radar-based FRP has potential to fill gaps and overcome satellite FRP biases occurring during extreme fire events

Supporting Information:

Supporting Information may be found in the online version of this article.

Correspondence to:

P. E. Saide,
saide@atmos.ucla.edu

Citation:

Saide, P. E., Krishna, M., Ye, X., Thapa, L. H., Turney, F., Howes, C., & Schmidt, C. C. (2023). Estimating fire radiative power using weather radar products for wildfires. *Geophysical Research Letters*, *50*, e2023GL104824. https://doi.org/10.1029/2023GL104824

Received 2 JUN 2023
Accepted 28 SEP 2023

Author Contributions:

Conceptualization: P. E. Saide
Data curation: P. E. Saide, L. H. Thapa, C. C. Schmidt
Formal analysis: P. E. Saide
Funding acquisition: P. E. Saide
Investigation: P. E. Saide, M. Krishna, L. H. Thapa
Methodology: P. E. Saide, M. Krishna, X. Ye
Project Administration: P. E. Saide
Resources: P. E. Saide
Software: P. E. Saide, M. Krishna
Supervision: P. E. Saide, X. Ye, F. Turney

1. Introduction

Radiant energy emitted from fires, usually referred to as Fire Radiative Energy (FRE), and its instantaneous counterpart, Fire Radiative Power (FRP) (Wooster & Zhang, 2004), have been found to be highly correlated with fuel mass loss and smoke concentrations, and thus have been used to estimate smoke emissions (Freeborn et al., 2008; Ichoku et al., 2008; Wooster, 2002). Spaceborne imagers are able to provide accurate FRP estimates (Wooster et al., 2005), which are used to derive trace gas and aerosol emissions from fires with global coverage (e.g., Darmenov and da Silva, 2015; Ichoku & Ellison, 2014; Kaiser et al., 2012). FRP and derived emissions are used in a variety of applications ranging from air quality forecasts (Ye et al., 2021) and atmospheric composition reanalysis (Buchard et al., 2017; Inness et al., 2019) to smoke impacts on health (O'Neill et al., 2021) and the influence on the earth's radiative budget (Carter et al., 2020). While most applications have used FRP retrievals from low-earth orbiting (LEO) satellites to provide daily emission estimates, FRP from a new generation of geostationary (GEO) sensors has been shown to be effective at capturing smoke in finer temporal resolutions (Wiggins et al., 2020) and led to the development of hourly smoke emissions estimates combining LEO and GEO data (Li et al., 2022).

While FRP derived emissions are extremely useful, they do come with associated uncertainties. For instance, FRP retrievals are unreliable or not possible when the fire is blocked by clouds (Schmidt et al., 2010). Additionally, it has been found that smoke emissions are generally underpredicted for extreme fire events (Saide et al., 2015; van

Validation: P. E. Saide
Visualization: P. E. Saide, L. H. Thapa
Writing – original draft: P. E. Saide
Writing – review & editing: P. E. Saide, M. Krishna, X. Ye, L. H. Thapa, F. Turney, C. Howes

der Velde et al., 2021), with potential causes including instrument saturation, the FRP algorithm not being able to find non-fire pixels needed for the retrievals, and obscuration by thick smoke or fire-generated clouds such as pyro-cumulus and pyro-cumulonimbus (Justice et al., 2006; Li et al., 2021, 2022). Also, there are large uncertainties in nighttime GEO FRP (Li et al., 2022). Thus, alternative ways to derive FRP or smoke emissions at similar spatial and temporal resolutions are desirable to use as complimentary information.

Weather radars have been demonstrated as an effective tool to profile wildfire plumes due to their ability to detect pyrometeors, defined as lofted biomass burning debris typically above 1 mm in diameter (McCarthy et al., 2019). Some applications include determination of smoke injection height (Jones & Christopher, 2009), speciation of pyrometeors (e.g., firebrands vs. ash) for spot fire risk prediction (McCarthy et al., 2020), estimating fire perimeter and rate of spread (Lareau, Donohoe, et al., 2022), studying pyroconvection (Kingsmill et al., 2023; Peterson et al., 2022) and fire-generated tornadic vortices (Lareau, Nauslar, et al., 2022), and investigating the microphysics, thermodynamics, and fire behavior feedback of wildfire plumes (McCarthy et al., 2019). While efforts have explored associations between fire area and radar plume area (Price et al., 2018), to our knowledge, there have been no studies connecting FRP or smoke emissions to weather radar retrievals.

This work investigates the potential for weather radars to estimate FRP, which can be further used to estimate smoke emissions. The following sections describe the FRP and weather radar products used, as well as methods to isolate pyrometeor signals from other phenomena and to integrate radar retrievals representing a fire. We show results comparing FRP and radar products for multiple fires, discuss sources of discrepancy, and outline conclusions, recommendations for usage, and future directions.

2. Materials and Methods

2.1. Weather Radar Products

Data from NOAA's Next Generation Weather Radar (NEXRAD) system were used. The NEXRAD Weather Surveillance Radar-1988 Doppler (WSR-88D) network consists of 160 S-band polarimetric radars across the US (Saxion et al., 2011; Serafin & Wilson, 2000), shown for the western US in Figure S1 in Supporting Information S1. Scans are performed every 4–12 min, a similar temporal resolution as the satellite FRP scans. Level II data corresponding to radar reflectivity, correlation coefficient, spectrum width, and radial velocity was used. The data was re-gridded to a cartesian grid of 1×1 km^2 horizontal resolution and ~500 m vertical resolution over the domains shown in Figure S2 in Supporting Information S1 using the Python ARM Radar Toolkit (Py-ART) (Helmus & Collis, 2016). This was done to be able to search data over vertical columns and to aggregate data across equally spaced grids. Radars used for each fire are listed in Table S1 in Supporting Information S1.

The lowest grid cell that the radars can sense without being blocked by topography was determined using the radar locations and high-resolution topography (USGS database at 1/3 arc-second) averaged within the radar grid cells (contours in Figure S2 in Supporting Information S1), which we refer to as "base" data. "Composite" data correspond to variables extracted at the level of maximum radar reflectivity. These extractions were performed after selecting data that had a larger potential to be associated with pyrometeors. The criteria were a minimum reflectivity of 10 dBZ and correlation coefficient between 0.2 and 0.9 starting from the base level up to a height where one of the conditions was not met. These filters are based on previous work (Jones & Christopher, 2009) and reduce the possibility of including reflectivity enhancements that are at altitude and also removing rain and drizzle echoes, which tend to show correlation coefficient greater than 0.9 (Liu & Chandrasekar, 2000). Correlation coefficient for pyrometeors tends to be below 0.8 (Melnikov et al., 2008; Zrnic et al., 2020). Figures 1b and 1h shows examples of this processing, showing the pyrometeor plume is captured when it's present, but there are often other features included not related to the fire which are discussed in Section 3.1.

2.2. Fire Radiative Power

Data from the Advanced Baseline Imager (ABI) on the GOES-17 satellite are used as inputs in the Wildfire Automated Biomass Burning Algorithm (WFABBA) algorithm to derive FRP at ~5 min intervals (Schmidt, 2020; Schmidt et al., 2010) and are used in this study. Fire detections can be separated using quality flags into good quality ("processed" flag) data and other more uncertain retrievals (saturated, contaminated by cloud or smoke, and high/medium/low probability of fire) with most of them producing a FRP retrieval (Li et al., 2022). Here we

10.1029/2023GL104824

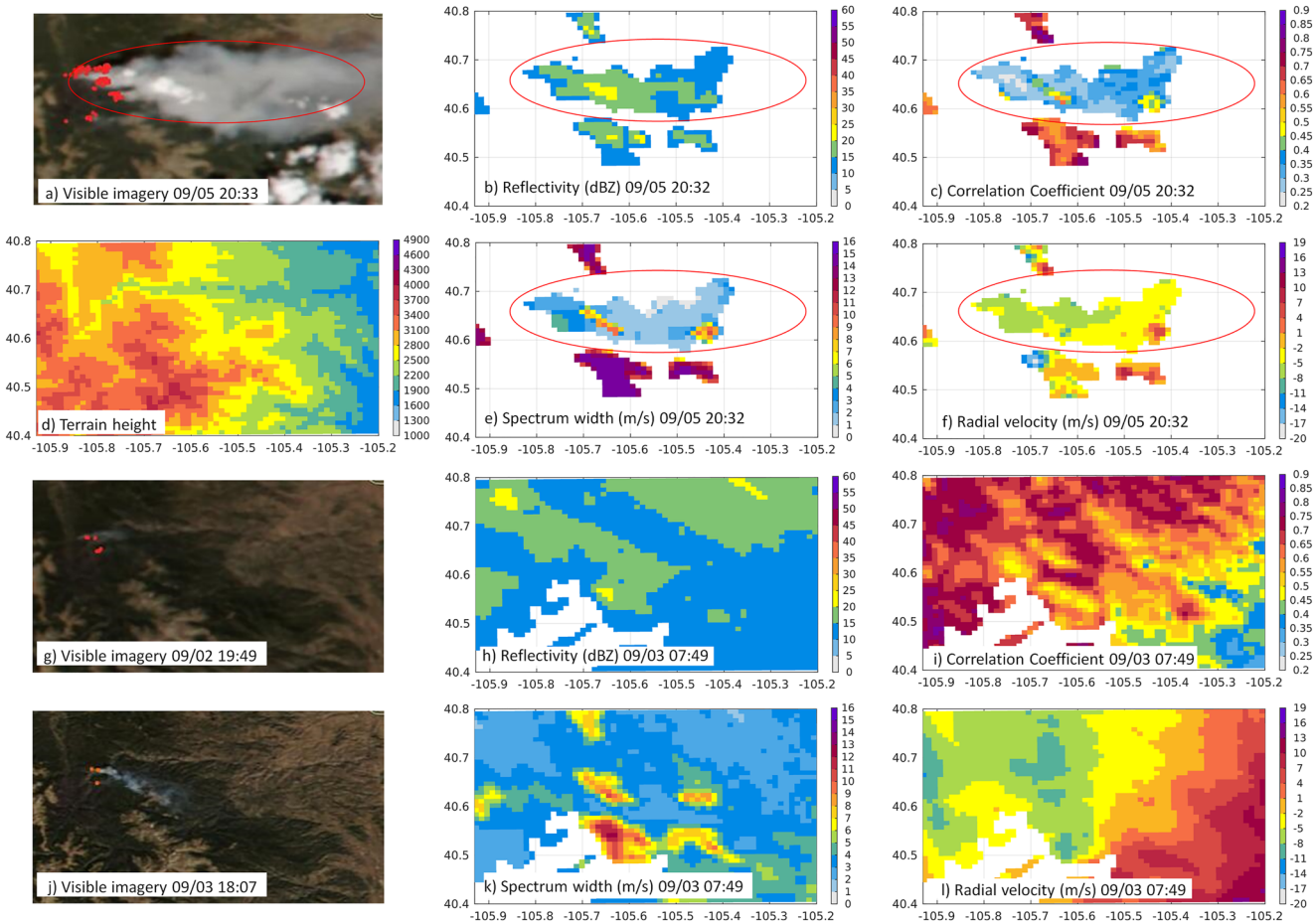

Figure 1. Maps of visible imagery (a, g, j), composite radar observables (middle and right columns), and terrain height (d) for the Cameron Peak fire domain. Fire detections for the corresponding overpass are shown on the visible imagery (a and g corresponds to NOAA-20 VIIRS, and j corresponds to Terra MODIS). The red oval in multiple panels represents the smoke/pyrometeor plume.

computed FRP for each scan (every ∼5 min) by adding all available FRP retrievals over a domain including the fire detections (Figure S2 in Supporting Information S1). FRP from each scan was classified into two groups, the high certainty ones where more than 50% of the fire detections were classified as good quality, and the rest with a lower degree of certainty. Then, hourly FRP was obtained by averaging all scans within 30 min of each hour. Hourly FRP values were also divided into two groups and considered to have a high degree of certainty when at least three of the scans used to calculate it were classified as high certainty. Night-time FRP were all classified as low certainty as is largely underestimated when compared to VIIRS FRP, with daytime values showing good performance (Li et al., 2022). The hourly high certainty data is used as the reference for all statistical analysis, but both groups are displayed in the time series.

2.3. Wildfires Studied

Nine fires that occurred during 2019 and 2020 in the western US were included in this study (Figure S1 and Table S1 in Supporting Information S1). These fires correspond to different environments including four different states, relatively flat terrain to complex mountain ranges (Figure S2 in Supporting Information S1), and at various distances from radar locations (30–180 km). Some fires were observed by two radars and in these cases the radar with better view was selected (noted on Table S1 in Supporting Information S1) depending on the day when it crossed topographical features. Some fires (e.g., Cameron Peak, Dolan) had multiple active periods separated by dormant conditions in which case different domains of FRP and radar products aggregation were chosen (shown in Figure S1 in Supporting Information S1). The fires studied are all considered major events, with final burned areas ranging from ∼18k (Williams Flats) to over 150k (Creek) hectares. However, since our analysis focuses

on the hourly evolution for fires, multiple periods of low intensity burning are included where FRP is close to the lower detection limit of ABI (~25 MW), allowing us to cover a wide range of FRP values (~4 orders of magnitude).

2.4. Associating Weather Radar Products to FRP

FRP has been found to be proportional to trace gas and aerosol emissions from fires (see Section 1), and thus it is reasonable to think that FRP and pyrometeor emissions are positively correlated. However, it is unknown if this relationship is linear (like for smoke emissions) or non-linear, since not all biomass burning debris may be suspended as pyrometeors (e.g., some ash remains on the ground) and that the fraction and size distribution that is suspended might be a function of fire behavior and environmental conditions (Ward, 1990).

Weather radars measure reflectivity (Z, mm^6 m^{-3}) which has been used to estimate rainfall rate (R, mm/h) using the Z-R relationship $Z = A\,R^b$, where A and b are empirically determined constants (Stout & Mueller, 1968). The power-law form of the Z-R relationship can be derived theoretically by assuming an exponential drop size distribution and expressing Z, R, and the drop terminal velocity as a function of this distribution (Burgess & Ray, 1986). In an analogous way, if the size distribution of pyrometeors was known, it could be used to derive the form of the relationship between reflectivity and pyrometeor fall rate. However, the underlying distribution of pyrometeor number concentration has not been established (McCarthy et al., 2019). Thus, here we test two plausible assumptions. First, an exponential distribution is assumed motivated by the linearity in the log-log space found by multiple studies measuring pyrometeors in-situ (Kingsmill et al., 2023; Peterson et al., 2022; Radke et al., 1991), in which case a relationship of the form of Z-R can be assumed. As a priori there is no information on what A and b should be for pyrometeors, for simplicity and to investigate the fit to FRP we use the Marshall and Palmer (1948) relationship ($Z = 200\,R^{1.6}$) typically used for stratiform rain, referring to it as "equivalent rainfall." Second, a log-normal distribution is assumed motivated by the similarity of aerosol size distributions with that of wood ash size distributions (Fusade et al., 2019; Grau et al., 2015), which is believed to be the dominant fraction of pyrometeors (McCarthy et al., 2019). In the log-normal case, it can be shown that a linear relationship between Z and R rate is obtained (Text S1 in Supporting Information S1), and thus we assume Z and pyrometeor fall rate are proportional.

Finally, due to mass conservation and assuming pyrometeor falling happens in timescales shorter than an hour, we assume that the pyrometeor emission rate can be approximated by the fall rate integrated spatially over the whole pyrometeor plume. A caveat of this assumption is that this integration includes the leading portion of the plume characterized by pyrometeor lofting. This region is driven by the fire-generated updrafts that are often >10 m/s and where pyrometeor fall velocities are considered negligible (Clements et al., 2018; Kingsmill et al., 2023). Thus, this lofting region is expected to be a small fraction of the overall plume area as it will take much longer for the pyrometeors to fall than to be lofted and thus its inclusion is not expected to impact the integration considerably.

In summary, we investigate relationship of the form:

$$\mathrm{FRP} = F\left(\sum_{\mathrm{plume}} Z\right)$$

where F is a function to be determined by the analysis. While this equation assumes a log-normal size distribution, Z is replaced by R when using equivalent rainfall rate for the exponential size distribution assumption. In other words, we investigate the association between the radar derived products that are proxies for pyrometeor emission rate (integrated equivalent rainfall and reflectivity) and FRP. When integrating spatially for each scan, equivalent rainfall is multiplied by the grid cell area (1 km^2) resulting in units of m^3/h so results are independent of the grid size chosen, while the same is done for reflectivity resulting in units of mm^6/m. Similarly to FRP aggregation, values for all scans within each hour are averaged to obtain hourly values, which are in the same units as the per-scan values. There are examples of both composite and base scans used for rainfall estimation (e.g., Fulton et al., 1998; Zhang et al., 2011), so here we also test both for equivalent rainfall and reflectivity.

3. Results

3.1. Analysis for Individual Fires

The Williams Flats fire occurred on terrain conditions that are relatively of low complexity (Figure S2l in Supporting Information S1), with a nearby radar (80 km), and with little blockage from topographic features

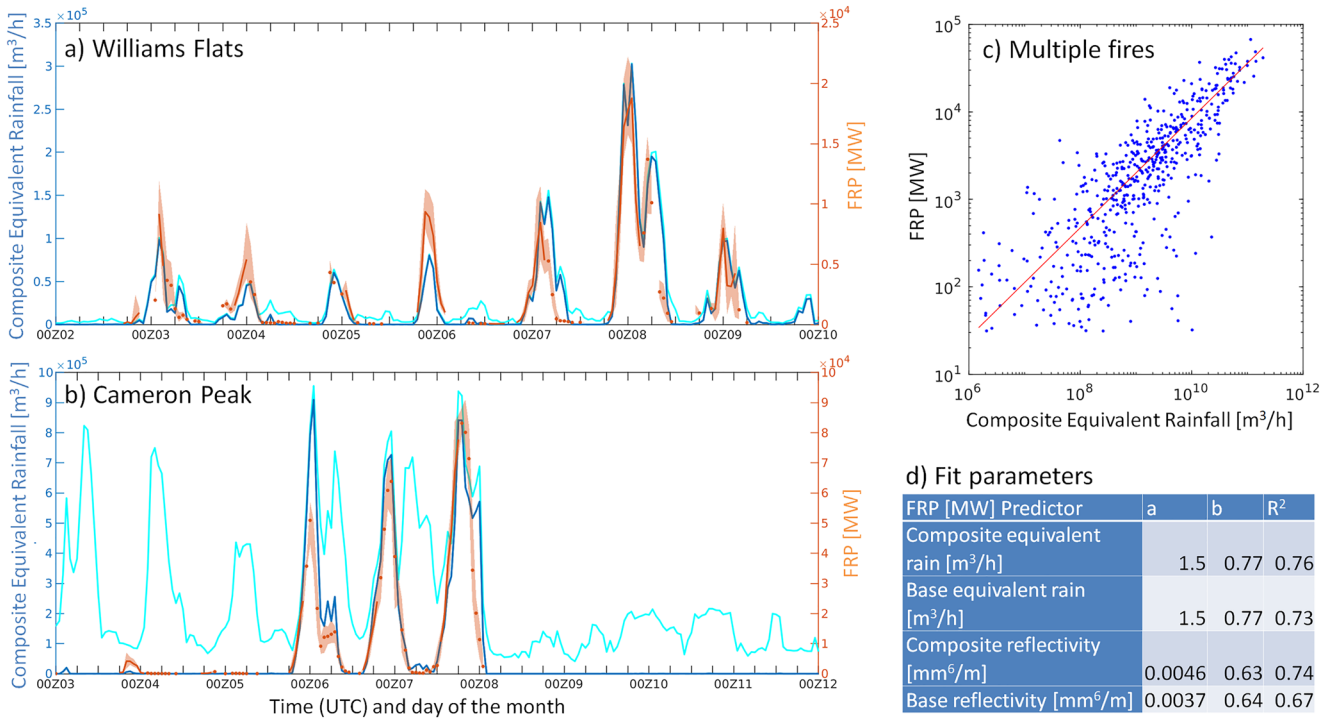

d) Fit parameters

FRP [MW] Predictor	a	b	R^2
Composite equivalent rain [m³/h]	1.5	0.77	0.76
Base equivalent rain [m³/h]	1.5	0.77	0.73
Composite reflectivity [mm⁶/m]	0.0046	0.63	0.74
Base reflectivity [mm⁶/m]	0.0037	0.64	0.67

Figure 2. Left panels: Hourly averages of integrated composite equivalent rain (blue and cyan, left axis) and FRP (red, right axis) for the Williams Flats fire (August 2019) and Cameron Peak fire (September 2020). The cyan and blue lines represent composite rain aggregated before and after filtering radar data using the machine learning classifier. The red solid lines and dots represent FRP with higher and low degree of certainty, respectively (see Section 2.2). The red-shaded polygons represent the range between the maximum and minimum FRP values over each hour. (c) Scatterplot of integrated composite rain (after filtering) and FRP for multiple fires (see main text). The red line represents a power law fit. (d) Parameters of the power-law fits (FRP = $a\,X^b$) for multiple radar observables (X).

(290 m on average, the lowest within the fires studied). Thus, it allows us to assess associations between FRP and integrated radar products under optimal conditions. Additionally, it's a well-studied fire as the FIREX-AQ field campaign sampled it multiple times (Warneke et al., 2023; Ye et al., 2021). Figure 2a shows a strong association between the higher certainty FRP and composite equivalent rain (R^2 of 0.85 for the linear fit), with the correlation also being strong for the other integrated radar products (0.81–0.83 R^2). In some periods of high FRP values, the FRP time series shows multiple gaps which are due to cloud cover (based on satellite imagery) where the radar product provides retrievals that could be used to fill in these gaps. The Williams Flats fire generated multiple pyro-cumulonimbus around 06 UTC on 8 September and 00 UTC on 9 September (Peterson et al., 2022) which could contribute to FRP blockage and result in the apparent overprediction of composite equivalent rain during these times.

Although filters were applied to isolate pyrometeor signals (Section 2.1), this was not sufficient for the Cameron Peak fire as enhanced radar signals are found for periods with low and no fire activity (Figure 2b). These signals appear to be of two types. First, the ones that appear throughout the day adding a background level to the integrated radar products (Figure 2b) and that tend to be isolated features associated with topographic peaks (e.g., compare non-pyrometeor enhancements in Figure 1b to peaks in 1d). These features are likely associated to echoes from these peaks and we refer to them as ground-clutter (GC). Second, there are substantial enhancements that tend to happen only at nighttime and are limited to some days (e.g., Figure 2b, September 3–7), and are widespread across the domain (Figure 1h). These are likely associated to anomalous propagation (AP) due to superrefraction of the radar beam from ground targets happening under strong vertical gradients of temperature and moisture close to the surface that can be generated by nocturnal radiation cooling (Fulton et al., 1998; Zhang et al., 2011). These two phenomena (GC and AP) appear in the majority of the fires studied (Figure S3 and Table S1 in Supporting Information S1) and greatly contaminate the pyrometeor signals.

We observe that the radar products other than reflectivity (correlation coefficient, spectrum width and radial velocity) tend to show values for pyrometeors that are distinct from the signals for GC (Figures 1b, 1c, 1e,

and 1f) and AP (Figures 1h, 1i, 1k, and 1l). For instance, pyrometeors tend to have low correlation coefficients indicative of non-spherical particles, and low spectrum width away from the fire-generated updrafts representing settling particles not greatly affected by turbulence. Thus, we trained a machine learning model to classify 3D radar reflectivity as either corresponding to pyrometeors or not. We created a training set specifying times and regions within each radar domain that likely corresponded to pyrometeor and GC/AP (Table S2 in Supporting Information S1) by manually looking at maps of radar products, terrain height, and satellite imagery for each fire as shown in Figure 1. Note the training set corresponded to a small fraction of the data, for instance, 3 and 15 hr of pyrometeor and non-pyrometeor data, respectively, were used for the Cameron Peak period shown in Figure 2b. We used a logistic regression binary classifier implementing a stochastic gradient descent solver (Langford et al., 2009) available in Matlab through the "fitclinear" function (The MathWorks Inc, 2020). This algorithm generated similar results to other more advanced methods (e.g., support vector machines, random forest) but at a much lower computational cost when training and classifying. The values corresponding to pyrometeors and non-pyrometeors for each radar product often varied across fires, and thus a different classifier was trained for each fire, domain, and radar. The classifier was used for all grid cells that passed the initial filter (Section 2.1) and the ones classified as pyrometeors were used to recompute base and composite fields and the integrated equivalent rainfall and reflectivity. The classifier was effective at removing GC/AP for the Cameron Peak fire (Figure 2b, Figure S4 in Supporting Information S1) removing most non-pyrometeor signals for low fire activity and generally being effective for scenes with overlapping large fire activity and AP (e.g., September 6–7). Association between integrated radar products and FRP increased substantially after the application of the classifier (e.g., R^2 of the linear fit increased from 0.17 to 0.75 for Cameron Peak). This was generally the case for all other fires studied (Figure S3 in Supporting Information S1).

There are other reasons influencing the degradation in the association between FRP and integrated radar products. The Walker fire occurred in a valley surrounded by mountains (Figure S2k in Supporting Information S1) which block radar signals from the KBBX radar (Figure S1 in Supporting Information S1) missing most of the plume (not shown). The KRGX radar is less blocked, but it's elevated with respect to the valley floor where the fire occurred (2,528 m vs. 1,200–1,800 m). This geometry results in days of low fire activity and the decaying part of the diurnal cycle not being captured by the radar products (Figure S3l in Supporting Information S1). Despite this, days with stronger smoke activity are detected during periods of FRP gaps or low-certainty FRP (Figure S3l in Supporting Information S1), thus making it still complementary even under these conditions. Periods of the Creek fire also show the integrated radar products missing the decaying part of the diurnal cycle (Figure S3e in Supporting Information S1) as the fire was burning in the inner parts of the valley that increased chances of blocking (Figure S2e in Supporting Information S1). Another potential issue is that of elevated features passing over the fires that have values of radar products similar to pyrometeors, such as is the case of chaff (Kurdzo et al., 2023; Zrnić & Ryzhkov, 2004). The composite equivalent rain for the SCU fire shows a peak on Aug 20 around 00 UTC during a period of mostly high certainty FRP that's in a decaying phase. The National Reflectivity Mosaic (https://www.ncei.noaa.gov/maps/radar/) shows widespread enhanced reflectivity that moves through the region and over the SCU fire around 00 UTC (Figure S5 in Supporting Information S1). While this is an elevated feature, since the fire was intense during this period, it coupled vertically to the pyrometeor plume, significantly enhancing the integrated radar products. Thus, future work should integrate chaff classification algorithms (e.g., Kurdzo et al., 2017; Yu et al., 2016) to assess if these signals can be automatically removed.

A common feature occurring on multiple fires is that FRP values start being classified as low certainty during periods of extreme fire behavior (e.g., Figure 2b). One notable case is that of the CZU fire where no FRP was retrieved for 6 hr during the day of largest growth (Figures S2f and S3f in Supporting Information S1). Another extreme case is the Creek fire which burned ∼33k hectares during the first two days, and during this period FRP is mostly unavailable or has low certainty and appears to be drastically underpredicted (Figure S3d in Supporting Information S1). The integrated radar products show robust signals and have potential to provide FRP estimates during these periods, although this needs to be verified with future work.

3.2. Combining Multiple Fires

Multiple fires studied here were combined to assess if robust relationships can be derived to estimate FRP based on integrated radar products. The Walker and Creek fires and the period around 00 UTC on Aug 20 for SCU were left out for this calibration due to the issues discussed in Section 3.1. Also, only high certainty FRP data were used.

Figure 2c shows the scatterplot of the composite equivalent rain versus FRP, showing a relationship that appears linear in the log-log space for FRP values above ∼500 MW. A power-law fits the data well with a R^2 of 0.76. Similar R^2 values are obtained when using the other radar derived products (0.67–0.74, Figure 2d). The fact that a single relationship fits each of these data sets well when including fires that are diverse in terms of their region, fuels, topography, and radar coverage is very encouraging. Sensitivity of the power-law fit to the exclusion of each fire shows that the fit coefficients generally remain within the confidence range of the original fit parameters (Tables S3 and S4 in Supporting Information S1). Also, similar statistical metrics are obtained when using data from each fire to evaluate the power-law fits calibrated with and without these fires (Table S4 in Supporting Information S1), showing the robustness of the fits.

We find positive correlations between pyrometeor plume area and FRP (0.59 R^2 for the power-law fit, Table S3 in Supporting Information S1), which is consistent with previous results for plume area and fire area (Price et al., 2018) as FRP and burned area are often correlated (Thapa et al., 2022). However, the fits to FRP are significantly more skillful for the reflectivity/rain based metrics derived in this work (Table S3 in Supporting Information S1) and are recommended for future use. Also, the use of reflectivity/rain reduces errors for large plumes that might not be fully contained in analysis domain, as the reflectivity close to the fire for these cases goes up to 20–30 dBZ and thus are one to two orders of magnitude larger than the values on the edges (that approach ∼10 dBZ) that would weight much less when integrating over the plume.

The association between integrated radar products and FRP fades below 500 MW (Figure 2c). One explanation is that a certain level of lift is needed to generate pyrometeor particles, and thus highly variable environmental factors not associated with the fire might play a more important role for low intensity fires. Another contributor could be that pyrometeors from low intensity fires are more likely to be found close to the surface, increasing the chance for ground contamination. Thus, the usage of FRP radar estimates below 500 MW is not recommended. However, below 500 MW many of the issues making satellite FRP retrievals uncertain (e.g., instrument saturation, pyro-cumulonimbus or thick smoke obscuring detections) are less likely and can be used more reliably.

It is worth noting that for both equivalent rain and reflectivity the exponent of the power law fit is below 1 with a narrow confidence interval (Table S3 in Supporting Information S1). This can be interpreted as pyrometeor emissions having a superlinear relationship with FRP. This is reasonable, as FRP likely controls the production of potential pyrometeor particles linearly (as it is the case for smoke emissions, see introduction) but on top of that the chance for stronger updrafts increases with larger FRP (e.g., Thapa et al., 2022), which are expected to lift more and bigger particles and thus increasing pyrometeor emissions even more. Future work should use theory and physics-based models to provide further understanding on these relationships and to include the effects of regional meteorology on them.

While similar results are obtained for different radar products, composite variables tend to consistently show better statistical metrics compared to their base counterparts, including higher correlation, lower errors, and higher fraction within factor 2 (Table S3 in Supporting Information S1). Potential reasons include reducing ground artifacts when reflectivity maxima are elevated and better capturing large reflectivity peaks that might be associated to larger FRP. Thus, we recommend the usage of composite variables moving forward. On the other hand, there is no clear difference in whether equivalent rain or reflectivity should be integrated. This choice of variable was associated with the assumed pyrometeor size distribution which is unknown (Section 2.4), but for the purpose of this work, the choice seems to be playing only a minor role in the results.

4. Conclusions and Future Directions

In this work we build a framework to estimate hourly FRP using weather radar products and test it for multiple fires over the western US during 2019–2020. We hypothesize that FRP is expected to be proportional to radar products integrated across the pyrometeor plume. Without strong a priori assumptions, we test proportionality to different scan types (composite vs. base) and different radar products (equivalent rainfall and reflectivity). Strong correlations between FRP and integrated radar products are found for wildfires under favorable conditions of topography and radar location. However, spurious values appear for fires located in complex topography due to ground clutter (GC) and anomalous propagation (AP). We show that these values can be removed effectively when using a supervised machine learning algorithm capable of classifying retrievals as pyrometeor or non-pyrometeor based on manually selected training sets for each fire. Remaining potential issues include

blockage of radar beams by topography, fires occurring below the radar altitude, and features passing above the active fires that enhance radar echoes. When combining multiple fires, we find that a power-law fit can explain a large fraction of the variability of FRP (0.67–0.76 R^2) and can be used to estimate FRP effectively. While all radar products show similar skill, composite values consistently generate better results and are recommended for future use. While relationships are not valid for FRP <500 MW, they show potential to fill-in cloud-related gaps and to overcome satellite FRP biases occurring during extreme fire events.

Multiple assumptions were made in this work because there are gaps in the knowledge about pyrometeor properties. Areas of uncertainty include size distribution, speciation (e.g., ash, soil, firebrands, scorched canopy foliage), complex dielectric properties (McCarthy et al., 2019), and how these factors change with fire intensity and fuel type. Additionally, there is a gap of knowledge on the relationship between smoke and pyrometeor emission and how they relate to environmental factors (e.g., wind, humidity). Given that radar data is increasingly being used to characterize wildfires, is imperative that future work addresses these gaps. These could include intensive observational periods where smoke and pyrometeor properties are measured for fires ranging across different fuel and severity conditions. These measurements could be used to develop optical properties calculations for pyrometeors and validate models of pyrometeor emissions. We expect this improved knowledge to inform radar-based FRP estimates to reduce variability and improve skill.

These techniques have potential to be used in operational smoke forecasting systems to improve smoke emissions and injection height. However, a limitation to achieve this objective is the manual selection of data sets to train the machine learning algorithm to classify pyrometeors, which as shown is a crucial step to obtain reasonable skill for multiple fires. Thus, future work should explore ways to automate this process. Unsupervised machine learning has shown to be effective at classifying pyrometeor speciation using a similar set of radar products as in this work (McCarthy et al., 2020), and thus similar automated methods could be explored in future applications of radar-based FRP estimation. This process will be facilitated by algorithms automatically tracking fire evolution using active fire detections (Chen et al., 2022).

While radar-based FRP estimates show promise to improve upon current methods used during extreme fire conditions, the skill of these estimates was not verified here as there are no reliable FRP references for these conditions. Thus, this should be assessed by future work using alternative methods. One potential route is to use these new estimates to derive smoke emissions, use it as input for an atmospheric composition model predicting smoke, and evaluate its results against smoke observations. Finding this model has improved skill compared to simulations using satellite FRP as emission driver will support future use of this approach for extreme fire events. This work would be facilitated by the fact that multiple metrics for model evaluation of smoke predictions have been established using ground-based, airborne, and satellite observations (Ye et al., 2021), and because satellite smoke retrievals have been found to be accurate during periods of extreme fires as the ones studied here (Ye et al., 2022).

Conflict of Interest

The authors declare no conflicts of interest relevant to this study.

Data Availability Statement

GOES-17 ABI FRP data were acquired directly from the University of Wisconsin SSEC and can be found at https://ezid.cdlib.org/id/doi:10.15144/S4CC7K. NEXRAD data on AWS was accessed from https://registry.opendata.aws/noaa-nexrad. USGS elevation data was obtained from https://apps.nationalmap.gov/downloader/.

Acknowledgments
This work has been supported by the following Grants: NSF 2013461, NSF 2238338, NASA 80NSSC18K0629, NASA 80NSSC20K1650, NOAA NA18OAR4310107, and by funding from the Anthony and Jeanne Pritzker Family Foundation. We also acknowledge insightful comments from two anonymous reviewers that improved an initial version of this work substantially.

References

Buchard, V., Randles, C. A., da Silva, A. M., Darmenov, A., Colarco, P. R., Govindaraju, R., et al. (2017). The MERRA-2 aerosol reanalysis, 1980 onward. Part II: Evaluation and case studies. *Journal of Climate*, *30*(17), 6851–6872. https://doi.org/10.1175/jcli-d-16-0613.1

Burgess, D., & Ray, P. S. (1986). Principles of radar. *Mesoscale Meteorology and Forecasting*, 85–117. https://doi.org/10.1007/978-1-935704-20-1_6

Carter, T. S., Heald, C. L., Jimenez, J. L., Campuzano-Jost, P., Kondo, Y., Moteki, N., et al. (2020). How emissions uncertainty influences the distribution and radiative impacts of smoke from fires in North America. *Atmospheric Chemistry and Physics*, *20*(4), 2073–2097. https://doi.org/10.5194/acp-20-2073-2020

Chen, Y., Hantson, S., Andela, N., Coffield, S. R., Graff, C. A., Morton, D. C., et al. (2022). California wildfire spread derived using VIIRS satellite observations and an object-based tracking system. *Scientific Data*, *9*(1), 249. https://doi.org/10.1038/s41597-022-01343-0

Clements, C. B., Lareau, N. P., Kingsmill, D. E., Bowers, C. L., Camacho, C. P., Bagley, R., & Davis, B. (2018). The rapid deployments to wildfires experiment (RaDFIRE): Observations from the fire zone. *Bulletin of the American Meteorological Society*, *99*(12), 2539–2559. https://doi.org/10.1175/BAMS-D-17-0230.1

Darmenov, A., & da Silva, A. M. (2015). *The quick fire emissions dataset (QFED)—Documentation of versions 2.1, 2.2 and 2.4* (Vol. 38, p. 183). NASA/TM–2015–104606. Retrieved from https://gmao.gsfc.nasa.gov/pubs/docs/Darmenov796.pdf

Freeborn, P. H., Wooster, M. J., Hao, W. M., Ryan, C. A., Nordgren, B. L., Baker, S. P., & Ichoku, C. (2008). Relationships between energy release, fuel mass loss, and trace gas and aerosol emissions during laboratory biomass fires. *Journal of Geophysical Research*, *113*(D1), D01301. https://doi.org/10.1029/2007JD008679

Fulton, R. A., Breidenbach, J. P., Seo, D.-J., Miller, D. A., & O'Bannon, T. (1998). The WSR-88D rainfall algorithm. *Weather and Forecasting*, *13*(2), 377–395. https://doi.org/10.1175/1520-0434(1998)013<0377:TWRA>2.0.CO;2

Fusade, L., Viles, H., Wood, C., & Burns, C. (2019). The effect of wood ash on the properties and durability of lime mortar for repointing damp historic buildings. *Construction and Building Materials*, *212*, 500–513. https://doi.org/10.1016/j.conbuildmat.2019.03.326

Grau, F., Choo, H., Hu, J. W., & Jung, J. (2015). Engineering behavior and characteristics of wood ash and sugarcane bagasse ash. *Materials*, *8*(10), 6962–6977. https://doi.org/10.3390/ma8105353

Helmus, J. J., & Collis, S. M. (2016). The python ARM radar toolkit (Py-ART), a library for working with weather radar data in the python programming language. *Journal of Open Research Software*, *4*(1), 25. https://doi.org/10.5334/jors.119

Ichoku, C., & Ellison, L. (2014). Global top-down smoke-aerosol emissions estimation using satellite fire radiative power measurements. *Atmospheric Chemistry and Physics*, *14*(13), 6643–6667. https://doi.org/10.5194/acp-14-6643-2014

Ichoku, C., Martins, J. V., Kaufman, Y. J., Wooster, M. J., Freeborn, P. H., Hao, W. M., et al. (2008). Laboratory investigation of fire radiative energy and smoke aerosol emissions. *Journal of Geophysical Research*, *113*(D14), D14S09. https://doi.org/10.1029/2007jd009659

Inness, A., Ades, M., Agustí-Panareda, A., Barré, J., Benedictow, A., Blechschmidt, A. M., et al. (2019). The CAMS reanalysis of atmospheric composition. *Atmospheric Chemistry and Physics*, *19*(6), 3515–3556. https://doi.org/10.5194/acp-19-3515-2019

Jones, T. A., & Christopher, S. A. (2009). Injection heights of biomass burning debris estimated from WSR-88D radar observations. *IEEE Transactions on Geoscience and Remote Sensing*, *47*(8), 2599–2605. https://doi.org/10.1109/TGRS.2009.2014225

Justice, C., Giglio, L., Boschetti, L., Roy, D., Csiszar, I., Morisette, J., & Kaufman, Y. (2006). *MODIS fire products algorithm technical background document*. MODIS science team.

Kaiser, J. W., Heil, A., Andreae, M. O., Benedetti, A., Chubarova, N., Jones, L., et al. (2012). Biomass burning emissions estimated with a global fire assimilation system based on observed fire radiative power. *Biogeosciences*, *9*(1), 527–554. https://doi.org/10.5194/bg-9-527-2012

Kingsmill, D. E., French, J. R., & Lareau, N. P. (2023). In situ microphysics observations of intense pyroconvection from a large wildfire. *Atmospheric Chemistry and Physics*, *23*, 1–21. https://doi.org/10.5194/acp-23-1-2023

Kurdzo, J. M., Bennett, B. J., Cho, J. Y. N., & Donovan, M. F. (2023). Extended polarimetric observations of chaff using the WSR-88D weather radar network. *IEEE Transactions on Radar Systems*, *1*, 181–192. https://doi.org/10.1109/TRS.2023.3288093

Kurdzo, J. M., Bennett, B. J., Veillette, M. S., Smalley, D. J., Williams, E. R., & Donovan, M. F. (2017). WSR-88D chaff detection and characterization using an optimized hydrometeor classification algorithm. *18th Conf. on Aviation, Range, and Aerospace Meteorology*.

Langford, J., Li, L., & Zhang, T. (2009). Sparse online learning via truncated gradient. *Journal of Machine Learning Research*, *10*, 777–801.

Lareau, N. P., Donohoe, A., Roberts, M., & Ebrahimian, H. (2022). Tracking wildfires with weather radars. *Journal of Geophysical Research: Atmospheres*, *127*(11), e2021JD036158. https://doi.org/10.1029/2021JD036158

Lareau, N. P., Nauslar, N. J., Bentley, E., Roberts, M., Emmerson, S., Brong, B., et al. (2022). Fire-generated tornadic vortices. *Bulletin of the American Meteorological Society*, *103*(5), E1296–E1320. https://doi.org/10.1175/BAMS-D-21-0199.1

Li, F., Zhang, X., & Kondragunta, S. (2021). Highly anomalous fire emissions from the 2019–2020 Australian bushfires. *Environmental Research Communications*, *3*(10), 105005. https://doi.org/10.1088/2515-7620/ac2e6f

Li, F., Zhang, X., Kondragunta, S., Lu, X., Csiszar, I., & Schmidt, C. C. (2022). Hourly biomass burning emissions product from blended geostationary and polar-orbiting satellites for air quality forecasting applications. *Remote Sensing of Environment*, *281*, 113237. https://doi.org/10.1016/j.rse.2022.113237

Liu, H., & Chandrasekar, V. (2000). Classification of hydrometeors based on polarimetric radar measurements: Development of fuzzy logic and neuro-fuzzy systems, and in situ verification. *Journal of Atmospheric and Oceanic Technology*, *17*(2), 140–164. https://doi.org/10.1175/1520-0426(2000)017<0140:Cohbop>2.0.Co;2

Marshall, J. S., & Palmer, W. M. K. (1948). The distribution of raindrops with size. *Journal of the Atmospheric Sciences*, *5*(4), 165–166. https://doi.org/10.1175/1520-0469(1948)005<0165:Tdorws>2.0.Co;2

McCarthy, N., Guyot, A., Dowdy, A., & McGowan, H. (2019). Wildfire and weather radar: A review. *Journal of Geophysical Research: Atmospheres*, *124*(1), 266–286. https://doi.org/10.1029/2018jd029285

McCarthy, N. F., Guyot, A., Protat, A., Dowdy, A. J., & McGowan, H. (2020). Tracking pyrometeors with meteorological radar using unsupervised machine learning. *Geophysical Research Letters*, *47*(8). https://doi.org/10.1029/2019GL084305

Melnikov, V. M., Zrnic, D. S., Rabin, R. M., & Zhang, P. (2008). Radar polarimetric signatures of fire plumes in Oklahoma. *Geophysical Research Letters*, *35*(14), L14815. https://doi.org/10.1029/2008GL034311

O'Neill, S., Diao, M., Raffuse, S., Al-Hamdan, M., Barik, M., Jia, Y., et al. (2021). A multi-analysis approach for estimating regional health impacts from the 2017 northern California wildfires. *Journal of the Air & Waste Management Association*, *71*(7), 791–814. https://doi.org/10.1080/10962247.2021.1891994

Peterson, D. A., Thapa, L. H., Saide, P. E., Soja, A. J., Gargulinski, E. M., Hyer, E. J., et al. (2022). Measurements from inside a thunderstorm driven by wildfire: The 2019 FIREX-AQ field experiment. *Bulletin of the American Meteorological Society*. https://doi.org/10.1175/bams-d-21-0049.1

Price, O. F., Purdam, P. J., Williamson, G. J., & Bowman, D. M. J. S. (2018). Comparing the height and area of wild and prescribed fire particle plumes in south-east Australia using weather radar. *International Journal of Wildland Fire*, *27*(8), 525–537. https://doi.org/10.1071/WF17166

Radke, L. F., Hegg, D. A., Hobbs, P. V., Nance, J. D., Lyons, J. H., Laursen, K. K., et al. (1991). Particulate and trace gas emissions from large biomass fire in North America. In J. S. Levine (Ed.), *Global biomass burning: Atmospheric, climatic, and biospheric implications* (pp. 209–216). The MIT Press.

Saide, P. E., Peterson, D., da Silva, A., Anderson, B., Ziemba, L. D., Diskin, G., et al. (2015). Revealing important nocturnal and day-to-day variations in fire smoke emissions through a multiplatform inversion. *Geophysical Research Letters*, *42*, 2015GL063737. https://doi.org/10.1002/2015gl063737

Saxion, D., Ice, R., Schlatter, P., Boydstun, O., Heck, A., Chrisman, J., et al. (2011). New science for the WSR-88D: Validating the dual polarization upgrade. In *27th international conference on interactive information systems processing for meteorology, oceanography, and hydrology* (pp. 22–27).

Schmidt, C. (2020). Chapter 13 - Monitoring fires with the GOES-R series. In S. J. Goodman, T. J. Schmit, J. Daniels, & R. J. Redmon (Eds.), *The GOES-R series* (pp. 145–163). Elsevier.

Schmidt, C., Hoffman, J., Prins, E., & Lindstrom, S. (2010). GOES-R advanced baseline imager (ABI) algorithm theoretical basis document for fire/hot spot characterization, version 2.0, NOAA, Silver Spring, Md, NOAA NESDIS. *Cent. Satell. Appl. Res*.

Serafin, R. J., & Wilson, J. W. (2000). Operational weather radar in the United States: Progress and opportunity. *Bulletin of the American Meteorological Society*, *81*(3), 501–518. https://doi.org/10.1175/1520-0477(2000)081<0501:OWRITU>2.3.CO;2

Stout, G. E., & Mueller, E. A. (1968). Survey of relationships between rainfall rate and radar reflectivity in the measurement of precipitation. *Journal of Applied Meteorology and Climatology*, *7*(3), 465–474. https://doi.org/10.1175/1520-0450(1968)007<0465:SORBRR>2.0.CO;2

Thapa, L. H., Ye, X., Hair, J. W., Fenn, M. A., Shingler, T., Kondragunta, S., et al. (2022). Heat flux assumptions contribute to overestimation of wildfire smoke injection into the free troposphere. *Communications Earth & Environment*, *3*(1), 236. https://doi.org/10.1038/s43247-022-00563-x

The MathWorks Inc. (2020). *MATLAB version: 9.9.0 (R2020b)*. The MathWorks Inc.

van der Velde, I. R., van der Werf, G. R., Houweling, S., Maasakkers, J. D., Borsdorff, T., Landgraf, J., et al. (2021). Vast CO_2 release from Australian fires in 2019–2020 constrained by satellite. *Nature*, *597*(7876), 366–369. https://doi.org/10.1038/s41586-021-03712-y

Ward, D. E. (1990). Factors influencing the emissions of gases and particulate matter from biomass burning. In J. G. Goldammer (Ed.), *Fire in the tropical biota: Ecosystem processes and global challenges* (pp. 418–436). Springer Berlin Heidelberg.

Warneke, C., Schwarz, J. P., Dibb, J., Kalashnikova, O., Frost, G., Al-Saad, J., et al. (2023). Fire influence on regional to global environments and air quality (FIREX-AQ). *Journal of Geophysical Research: Atmospheres*, *128*(2), e2022JD037758. https://doi.org/10.1029/2022JD037758

Wiggins, E. B., Soja, A. J., Gargulinski, E., Halliday, H. S., Pierce, R. B., Schmidt, C. C., et al. (2020). High temporal resolution satellite observations of fire radiative power reveal link between fire behavior and aerosol and gas emissions. *Geophysical Research Letters*, *47*(23), e2020GL090707. https://doi.org/10.1029/2020GL090707

Wooster, M. J. (2002). Small-scale experimental testing of fire radiative energy for quantifying mass combusted in natural vegetation fires. *Geophysical Research Letters*, *29*(21), 2027. https://doi.org/10.1029/2002gl015487

Wooster, M. J., Roberts, G., Perry, G. L. W., & Kaufman, Y. J. (2005). Retrieval of biomass combustion rates and totals from fire radiative power observations: FRP derivation and calibration relationships between biomass consumption and fire radiative energy release. *Journal of Geophysical Research*, *110*(D24), D24311. https://doi.org/10.1029/2005jd006318

Wooster, M. J., & Zhang, Y. H. (2004). Boreal forest fires burn less intensely in Russia than in North America. *Geophysical Research Letters*, *31*(20), L20505. https://doi.org/10.1029/2004GL020805

Ye, X., Arab, P., Ahmadov, R., James, E., Grell, G. A., Pierce, B., et al. (2021). Evaluation and intercomparison of wildfire smoke forecasts from multiple modeling systems for the 2019 Williams Flats fire. *Atmospheric Chemistry and Physics*, *21*(18), 14427–14469. https://doi.org/10.5194/acp-21-14427-2021

Ye, X., Deshler, M., Lyapustin, A., Wang, Y., Kondragunta, S., & Saide, P. (2022). Assessment of satellite AOD during the 2020 wildfire season in the western U.S. *Remote Sensing*, *14*(23), 6113. https://doi.org/10.3390/rs14236113

Yu, J., Lee, H., Jeong, Y., & Kim, S. (2016). Identifying chaff echoes in weather radar data using tree-initialized fuzzy rule-based classifier. In *2016 IEEE international conference on fuzzy systems (FUZZ-IEEE)* (pp. 2317–2324).

Zhang, J., Howard, K., Langston, C., Vasiloff, S., Kaney, B., Arthur, A., et al. (2011). National mosaic and multi-sensor QPE (NMQ) System: Description, results, and future plans. *Bulletin of the American Meteorological Society*, *92*(10), 1321–1338. https://doi.org/10.1175/2011BAMS-D-11-00047.1

Zrnic, D., Zhang, P., Melnikov, V., & Mirkovic, D. (2020). Of fire and smoke plumes, polarimetric radar characteristics. *Atmosphere*, *11*(4), 363. https://doi.org/10.3390/atmos11040363

Zrnić, D. S., & Ryzhkov, A. V. (2004). Polarimetric properties of chaff. *Journal of Atmospheric and Oceanic Technology*, *21*(7), 1017–1024. https://doi.org/10.1175/1520-0426(2004)021<1017:PPOC>2.0.CO;2

References From the Supporting Information

Aitchison, J., & Brown, J. (1957). *The lognormal distribution*. University of Cambridge, Department of Applied Economics Monograph 5. Cambridge University Press.

Grainger, R. G. (2022). Some useful formulae for aerosol size distributions and optical properties. Retrieved from https://eodg.atm.ox.ac.uk/user/grainger/research/aerosols.pdf

Seinfeld, J. H., & Pandis, S. N. (2016). *Atmospheric chemistry and physics: From air pollution to climate change*. John Wiley & Sons.

Serio, M. A., Carollo, F. G., & Ferro, V. (2019). Raindrop size distribution and terminal velocity for rainfall erosivity studies. A review. *Journal of Hydrology*, *576*, 210–228. https://doi.org/10.1016/j.jhydrol.2019.06.040